

Control of estuarine sediment dynamics by interactions between currents and waves at several scales

Malcolm O. Green ^{a,*}, Kerry P. Black ^{a,b}, Carl L. Amos ^c

^a National Institute of Water and Atmospheric Research, Ltd., P.O. Box 11-115, Hamilton, New Zealand

^b Department of Earth Sciences, University of Waikato, Private Bag 3105, Hamilton, New Zealand

^c Geological Survey of Canada – Atlantic, Bedford Institute of Oceanography, P.O. Box 1006, Dartmouth, NS B2Y 4A2, Canada

Received 24 July 1996; accepted 1 May 1997

Abstract

The effect of interactions between continuous (tidal currents) and intermittent (waves) processes on sediment dynamics and transport is addressed by presenting detailed field measurements of waves, boundary-layer currents and suspended sediment from an estuarine channel and an adjacent intertidal sandflat in Manukau Harbour, New Zealand. The aim is to determine in what ways it is necessary to couple waves and currents in numerical models, and thereby put limits on the fundamental structure of process-based estuarine sediment transport models. Waves were important on the intertidal flat: turbidity switched on and off with the appearance and disappearance of waves; wave groups dominated entrainment of bed sediment; a wave–current boundary-layer model explained measured bed shear stress and hydraulic roughness; and the measured near-bed time-averaged suspended-sediment concentration was mostly well predicted by a pure-wave model. Both the waves themselves and wave-related processes varied markedly over the tidal cycle. The variation in the former (principally changes in wave height) was related to changes in fetch caused by the harbour-wide emergence and submergence of intertidal regions. The variation in the latter was related to changes in water depth relative to the wavelength of the waves, which controlled the penetration to the bed of wave-orbital currents. In addition to the variation over the tidal cycle in the ‘intensity’ of wave processes, there was also a change in ‘kind’, which occurred with the arrival at the measurement site of the ‘turbid fringe’, which is the narrow, highly turbid edge of the estuarine water body. The relationship between suspended-sediment concentration and wave-orbital velocity in the turbid fringe was radically different to the relationship in the estuarine water body proper, which suggests a change in dynamics, perhaps related to breaking waves. A ‘hybrid’ modelling approach is required, i.e. one that treats discrete events but resolves tidal-cycle-scale variation within the event. There is a need to resolve the variation in the wave train over the tidal cycle and the penetration to the bed of wave-orbital motions, both of which could only be done adequately within an estuary tidal model. In contrast to the situation on the intertidal flat where waves intermittently entrained sediment, sediment transport in the channel was continuous, driven by tidal currents. To predict sediment flux in the channel we need to know the upstream sediment-transporting capacity of the flow (including that contributed by waves), the character of the bed sediment, and the sediment-settling time

Corresponding author. Fax: +64 (7) 856-0151; e-mail: m.green@niwa.cri.nz

scale. These factors confounded even the simplest notion of flood and ebb dominance, which frequently has been applied to understand estuarine morphodynamics. © 1997 Elsevier Science B.V.

Keywords: estuary; sediment transport; waves; currents

1. Introduction

In order to advance beyond conceptual understanding (e.g. 'sedimentation umbra', Kestner, 1975; 'equilibrium capacity' of an enclosed tidal water body, Amos and Tee, 1989) it is necessary to develop numerical models that link and integrate processes at all scales and throughout the estuary. Field measurements are required to identify processes and to guide the way processes are represented in models. The measurements presented herein, which have been obtained using an instrumented tripod that to date has found application more commonly in open-coast environments (continental shelf and surf zone), will be useful in showing which processes are relevant and how they should be represented in models. Such models should ultimately have great utility in applied problems and in answering fundamental scientific questions such as how channels, which act principally as conduits of sediment, and intertidal flats, which act principally as repositories of sediment, actually exchange sediment.

The paradigm of net sediment transport in estuaries arising from asymmetric continuous processes is well established (e.g. settling and scour lag underneath tidal flows, Postma, 1967) but it is also known that wind waves have intermittent effects on turbidity, especially in shallower waters (e.g. Anderson, 1972; Ward et al., 1984; Shoellhamer, 1995). An important question, and one that has not been addressed previously, is how the continuous (tidal currents) and intermittent (waves) processes interact to control sediment dynamics.

Herein we present detailed field measurements of waves, boundary-layer currents and suspended sediment from a channel and from an adjacent intertidal sandflat in Manukau Harbour, New Zealand. Our aim is to identify and describe the ways in which sediment entrainment and transport are controlled by interactions between waves and

currents. The rationale is to determine in what ways it is necessary to couple waves and currents in a numerical model in order to produce accurate predictions of sediment entrainment and transport. The interpretation of this dataset will therefore put limits on the fundamental structure of process-based estuarine sediment transport models.

2. Location

The field site is in the eastern sector of the Manukau Harbour, which is a large (340 km²) estuary that empties into the Tasman Sea on the west coast of the North Island of New Zealand (Fig. 1a). The harbour is the western seaport for the city of Auckland. The tide range varies from >4 m at springs to ~1.5 m at neaps, and tidal currents can be strong ($\bar{U}_{100} > 2$ m/s) in places. A number of small streams flow into the harbour, but none contribute significant volumes of fresh-water or suspended sediment other than during exceptional events. Thus, the estuary is typically well-mixed vertically and circulation is dominated by the barotropic tide. A significant feature is that up to 40% of the area dries out at low tide (Heath et al., 1976), which profoundly affects generation of wind waves by the prevailing southwesterly winds. Fetches of up to 25 km are presented to southwesterly winds at high tide, at which times waves in excess of 1.5 m high may be generated in the central reaches. It is not known how much, if any, ocean swell penetrates the estuary.

The self-contained instrumented tripod 'RALPH' (operated by the Geological Survey of Canada) was deployed on an intertidal flat between Wiroa Island and Papakura Channel at 50 cm above LAT (lowest astronomical tide) in the eastern sector of the harbour near Auckland International Airport (Fig. 1b). The distance from the deployment site to the channel in a southwesterly direction was ~500 m. RALPH was situated

on the crest of a subtle linear bar, which is one of a field of such features that emerge from a shallow region bordering the intertidal flat to the west and southwest (Fig. 1b). The average spacing of the bars is 50 m, crest lengths vary between ~ 0.5 and 1 km, and average bar amplitude is ~ 5 cm. At high tide the fetch into the site under the prevailing southwesterly winds is 16 km, but at low tide the fetch is broken up by emerging sandbanks. The tidal current at the RALPH site floods to the east and ebbs to the southwest. In addition to RALPH, an InterOcean S4A current meter fitted with an infrared optical backscatter sensor (OBS) for measuring suspended-sediment concentration was deployed on the margin of Papakura Channel at ~ 5 m below LAT (Fig. 1b).

Dolphin (1992) described the morphology and sedimentology of the intertidal flat adjacent to Wiroa Island, and Dolphin et al. (1995) described sedimentary processes operating higher up the flat than the RALPH site. Unconsolidated sediments overlie grey and blue compacted silts and the depth of sand over the basement varies between 20 and 70 cm. In addition to the linear bars on the outer edge of the intertidal flat, there are low-amplitude multiple bars near the shoreline, the genesis of which is related to episodic wind-wave activity (Dolphin, 1992). In areas where the shoreline bars are present, sediment cover may be reduced and at some locations the basement may be exposed. Anaerobic sediments are typically encountered 1–2 cm below the surface, indicating that sediments above that depth are frequently reworked. Surface sediments were found by Dolphin to comprise 96% sand and 4% mud. The sand fraction consists of well-sorted, fine sand (median grain size of 0.2 mm). There is a very slight trend towards finer sands and a higher percentage of mud as the Papakura Channel is approached. The mean grain size of the bed sediment at the RALPH site is 0.1 mm. Muds may accumulate as a fine veneer after floods, but do not persist. The surface sediment is frequently moulded into small, symmetrical ripples approximately 1–2 cm high, 10–50 cm long, and with crests oriented shore-parallel. The ripple size, orientation and symmetry suggest that these are built by wave-orbital motions. In addition, the surface is marked in places by drainage channels,

'ray pits' (0.5–1.5-m-diameter by 10–30-cm-deep depressions) created by feeding eagle rays [*Myliobatis tenuicaudatus* (Hector)] and mounds where incipient *Zostera* colonies have promoted sedimentation.

3. Methods

Bursts are referred to by 'burst number'. Burst 0 began at 12:00, March 25, 1995, and subsequent burst numbers increment by 1 every half hour. There were several sensor malfunctions so the usable dataset is not continuous. In addition, fouling of optical backscatter sensors was severe, which resulted in much data being discarded. We are thus reduced to analysis of a few specific events here.

RALPH is a 2.5-m-high tripod equipped with an array of sensors for measuring waves, currents, suspended-sediment concentration (SSC) and bed-forms. RALPH was deployed on March 30, 1995, and finally recovered on May 16. Every hour on the hour two horizontal components of current velocity at three elevations ($z=97$, 48 and 17 cm above the seabed), SSC at five elevations ($z=177$, 97, 47, 22 and 7 cm) and pressure at two elevations ($z=150$ and 0 cm) were sampled at a 5-Hz rate and 4400 samples of each variable stored.

Currents were measured with electromagnetic sensors, which were calibrated in a flume. SSC was measured with optical backscatter sensors, which were calibrated in a turbidity tank with bed sediment from the deployment site prior to the experiment. Suspended-sediment samples taken periodically throughout the deployment were used to verify the laboratory calibration. Before applying the calibration to the raw output, the data were inspected for evidence of biofouling, which is indicated in the SSC signal by an exponentially rising 'floor', which is indicative of change in sensor offset, and fluctuations that decrease in amplitude, which is indicative of change in sensor gain. It is not possible to correct the data for effects of biofouling; therefore, a subjective estimate was made of when biofouling became significant, and data were discarded accordingly.

Pressure sensors read absolute pressure.

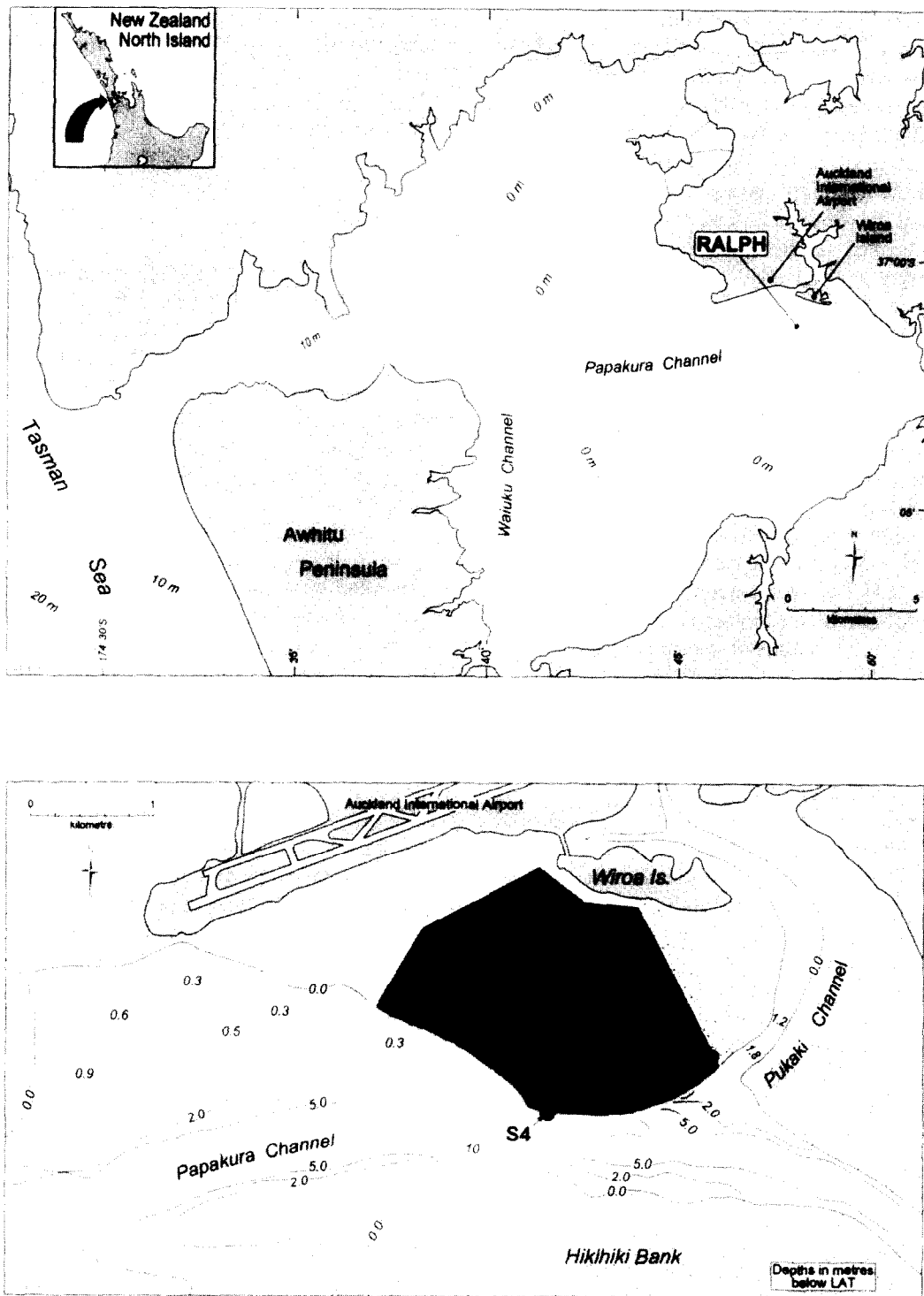
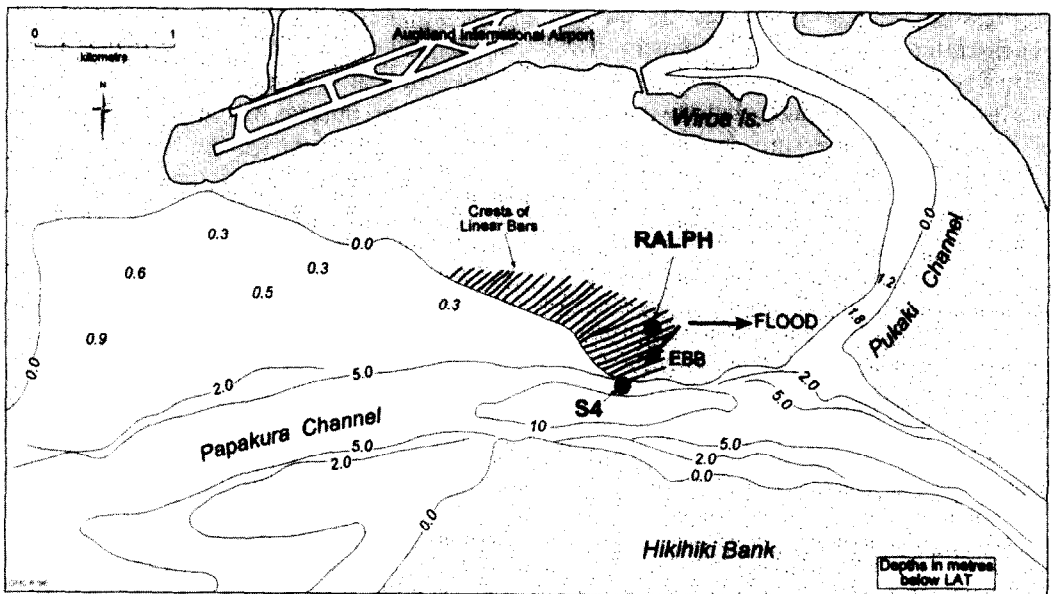
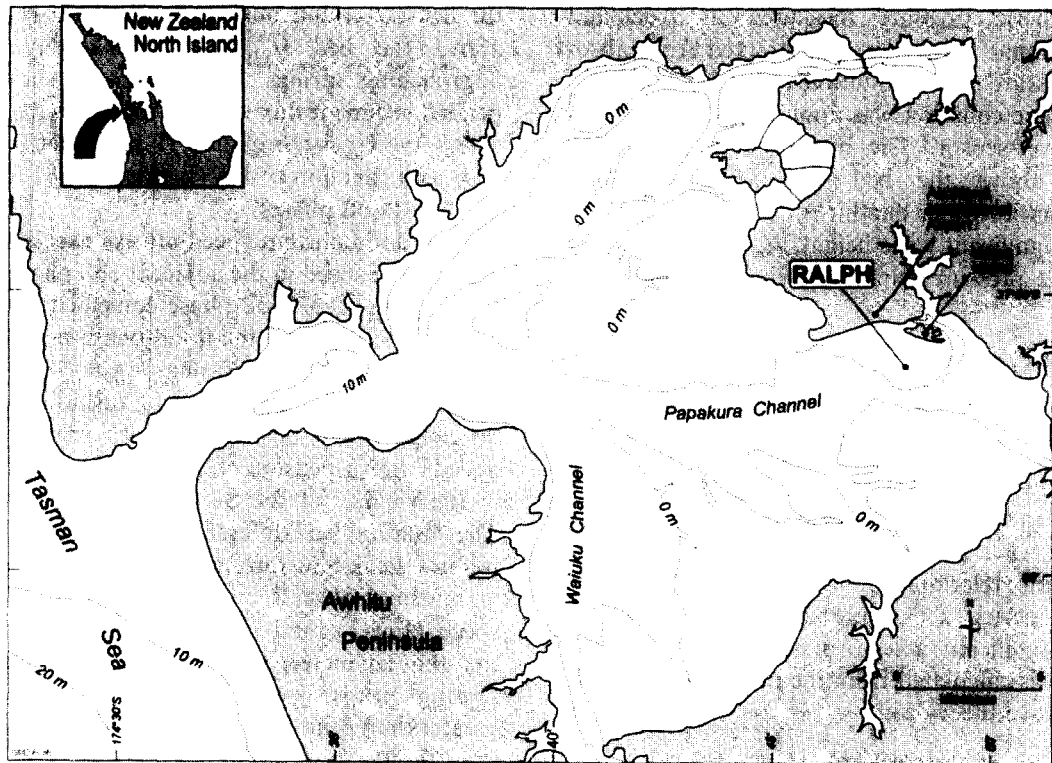


Fig. 1. (a) Manukau Harbour. (b) Deployment locations. Depths are in metres below LAT. The crests of the linear bars have been sketched from an aerial photograph taken at low tide. The depiction of the bar crests is truncated at the 0-m contour because the view of the seabed below 0-m depth was obscured by muddy water at the time of the photograph. RALPH was situated on the crest of a linear bar. The typical flood- and ebb-current directions at the RALPH site are shown. The S4 was on the margin of the Papakura Channel at ~5 m below LAT.



Atmospheric pressure measured at Auckland International Airport was subtracted from absolute pressure and a multiplier derived from the hydrostatic equation was applied to derive water-depth-over-sensor. The measured height of the sensor above the bed was added to yield (hydrostatic) water depth (h).

The significant wave height, H_{sig} , was estimated from the pressure data using linear wave theory as:

$$H_{\text{sig}} = \frac{4h_{\text{SD}}\cosh(k\bar{h})}{\cosh[k(z_p + \bar{h})]} \quad (1)$$

where h_{SD} is the standard deviation of the water depth h , z_p is the elevation of the pressure sensor relative to the burst-averaged water depth \bar{h} , and k is the wave number calculated using the linear dispersion relationship with \bar{h} and the mean spectral period \bar{T} (Longuet-Higgins, 1975). $U_{\text{sig},b}$ is the significant wave-orbital speed at the bed, which was calculated from the pressure data using linear wave theory as:

$$U_{\text{sig},b} = \frac{4\pi h_{\text{SD}}\cosh(k\bar{h})}{\bar{T}\sinh(k\bar{h})\cosh[k(z_p + \bar{h})]} \quad (2)$$

The S4A comprises an electromagnetic current meter, a pressure transducer (absolute) and an optical backscatter sensor. The instrument was mounted on a stainless-steel pole set into a concrete slab that sat on the seabed such that current was measured at $z = 90$ cm, pressure at 82.5 cm and SSC at 100 cm. The burst interval was 30 min, sampling interval 0.5 s, and burst duration 18 min. Pressure data were converted to depth by subtracting measured atmospheric pressure and applying the hydrostatic equation. Biofouling of the OBS was less of a problem in the channel than on the intertidal flat but still resulted in discard of a significant amount of data.

4. Results

4.1. Channel sediment transport

S4A data from the margin of Papakura Channel are presented in Fig. 2. The bottom panel shows \bar{h} , burst-averaged current speed at 90 cm above

the bed (\bar{U}_{90}) and burst-averaged SSC at 100 cm above the bed (\bar{C}_{100}) over a 7-day period approaching springs. The top panel shows suspended-sediment flux estimated as $\bar{U}_{90}\bar{C}_{100}$. Fig. 3 shows the cross-correlation (Γ) between \bar{U}_{90} and \bar{C}_{100} as a function of lag (Bendat, 1958) for both ebb and flood phases.

Peak flood current speed always exceeded peak ebb current speed in the adjacent ebb phases. Peak SSC during each flood phase coincided with peak current speed and as the flood-phase-peak current speed increased the flood-phase-peak SSC likewise increased. This suggests that turbidity on the flooding tide in the channel was primarily produced by resuspension of 'local' bed sediments (i.e. in the vicinity of the S4A) by the tidal current. The situation was different during ebbing tides, as follows. Peak SSC during each ebb phase occurred an average of half an hour after peak current speed (Fig. 3), and inspection of Fig. 2 suggests that that lag increased as springs were approached. During neaps, each ebb-phase-peak SSC was greater than peak SSC in the preceding flood phase even though peak ebb currents were slower than peak flood currents. During springs, ebb-phase-peak SSC was sometimes less than peak SSC in the preceding flood phase. This complexity suggests that turbidity on the ebbing tide cannot be explained wholly in terms of local resuspension. Advection of suspended sediment derived from an up-estuary source is the obvious alternative process that could account for the observations, in which case the composition of the sediment load might vary over the tidal cycle. We have no data to test that suggestion.

Multiplying SSC by horizontal current speed yields horizontal sediment flux, which at the S4A site in the channel was continuous, bidirectional and varied in magnitude with tidal stage. The channel margin would be classified as 'flood-dominated' in the normal sense, i.e. the peak flood current is faster than the peak ebb current, which gives the expectation of net up-estuary sediment transport because 'transport' is presumed to be a power function of velocity (e.g. Pethick, 1984; Jarvis and Riley, 1987). Flood-phase $\bar{U}_{90}\bar{C}_{100}$ always exceeded $\bar{U}_{90}\bar{C}_{100}$ in the adjacent ebb phases and integration of $\bar{U}_{90}\bar{C}_{100}$ over the period

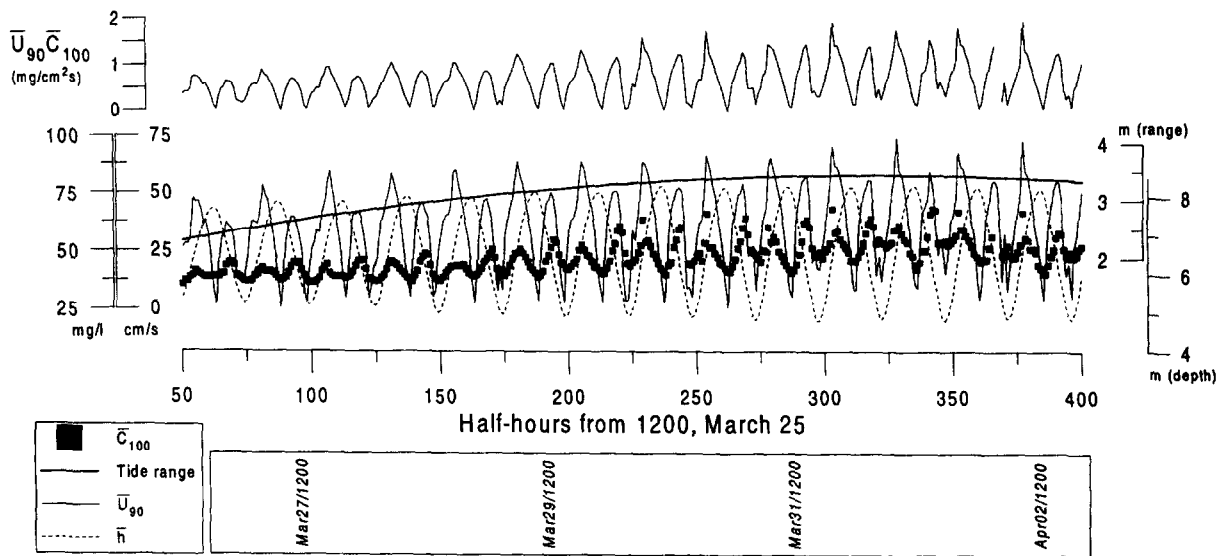


Fig. 2. Burst-averaged water depth (\bar{h}), current speed at 90 cm above the bed (\bar{U}_{90}), SSC at 100 cm above the bed (\bar{C}_{100}) and horizontal suspended-sediment flux estimated as $\bar{U}_{90}\bar{C}_{100}$ over a 7-day period approaching springs in Papakura Channel, 500 m to the west of the RALPH site on the intertidal flat.

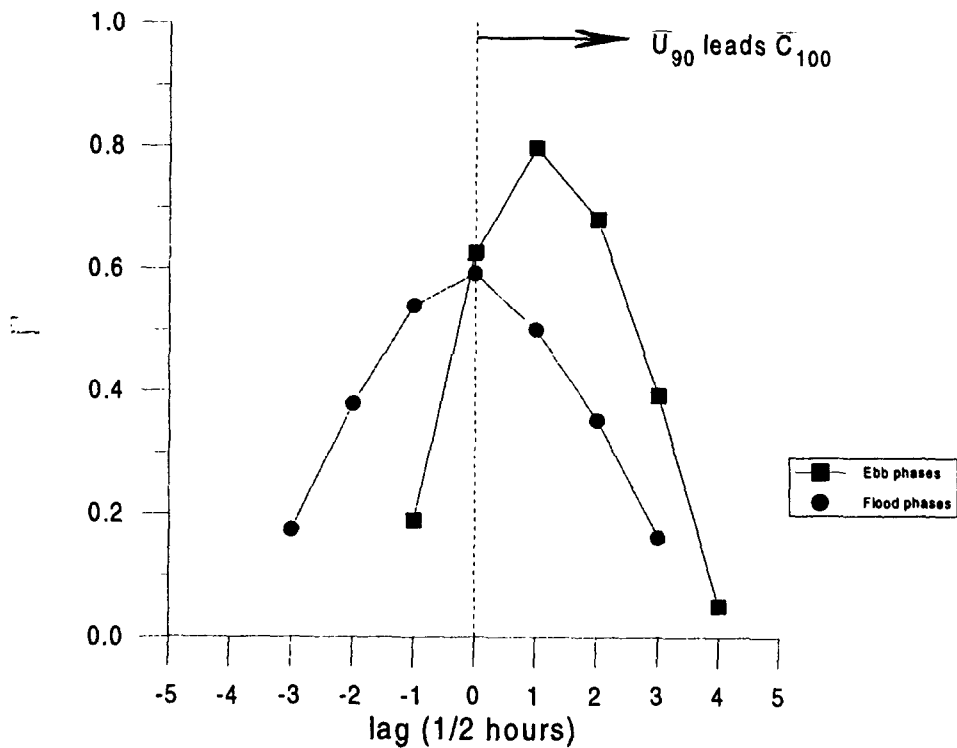


Fig. 3. The cross-correlation (Γ) between \bar{U}_{90} and \bar{C}_{100} as a function of lag for both ebb and flood phases in the Papakura Channel over the 7-day period shown in Fig. 2.

shown in Fig. 2 did yield a net up-estuary flux of sediment. However, since \bar{C}_{100} was apparently not always due solely to resuspension of local bed sediment, the flood/ebb-dominated concept is not totally applicable and thus the confirmation of the flood-dominated expectation may have been fortuitous.

It took three to four tidal cycles for turbidity in the channel to decrease back to normal levels after a relatively small storm in which the maximum H_{sig} in the channel was 40 cm. The net flux of sediment through the channel deployment site, estimated as $\bar{U}_{90}\bar{C}_{100}$, was directed up-estuary after the storm, meaning that the water column was cleared by some combination of settling and removal of sediment towards the head of the estuary. The 'excess' turbidity most likely derived from shallow intertidal flats under the action of waves, as described in the next section.

4.2. Intertidal-flat sediment transport

4.2.1. Control of turbidity by waves

On the intertidal flat, the change in turbidity accompanying development of waves was dramatic (Fig. 4). Shown on the left in Fig. 4 is the tide rising in bursts and on the right is SSC at 7 cm above the bed (C_7) on the intertidal flat. The top panel in Fig. 4 shows data from a flooding tide in calm conditions (burst numbers 896 to 904; morning of April 13), during which waves were virtually nonexistent and the water was clear. The bottom panel shows data from the next flooding tide (burst numbers 920 to 930; early evening of April 13), during which a moderate southwesterly wind (mean speed ~ 8 m/s) was raising groupy waves, which is evident from the depth time series. The change in turbidity was dramatic: near low tide, C_7 exceeded 600 mg/l at times and \bar{C}_7 was ~ 400 mg/l. Such concentrations are comparable with measurements from open-coast beaches (e.g. Beach and Sternberg, 1988; Black and Rosenberg, 1991). As the tide rose, \bar{C}_7 fell until the water had become clear again at high tide. Other sections of data show how quickly suspension is 'switched on' with the appearance of waves: between the end of burst 2154 and the start of burst 2156 (46 min) the wind changed from a 1.5-m/s northerly to a

10-m/s southwesterly, waves appeared, and \bar{C}_7 jumped from virtually zero to ~ 20 mg/l and then again to ~ 200 mg/l 1 h later.

The data demonstrate clearly that waves alone control turbidity on the intertidal flat, which is a profound contrast to the situation in the nearby Papakura Channel.

4.2.2. Local suspension of sediment versus advection of sediment from distant sources

Turbidity at the RALPH site was not always solely due to suspension of *local* bed sediment. For instance, burst-averaged SSC was virtually uniform over the bottom metre of the water column (i.e. $\bar{C}_7 \approx \bar{C}_{22} \approx \bar{C}_{97}$) during the period shown in Fig. 4 (bursts 920–930), which is not consistent with suspension of local fine sands, as shown by the following order-of-magnitude calculation. Assuming turbulence and vertical mixing are vertically invariant yields:

$$C_z = \bar{C}_0 e^{(z - \lambda_s)} \quad (3)$$

for the vertical time-averaged SSC profile under waves (Nielsen, 1984), where \bar{C}_0 is a reference concentration at the bed ($z=0$) and λ_s is a 'mixing length' equal to the ratio of sediment diffusivity and sediment settling velocity. Typically, λ_s is $O(10$ cm) for fine sands (e.g. Black and Rosenberg, 1991), meaning that C_z decays to about 40% of the reference value within $O(10$ cm) of the bed. That clearly was not the case for bursts 920 to 930 and indeed the uniform suspension implies a vanishingly small settling velocity, which is consistent with a very fine 'washload' that has been carried from a non-local source by the tidal current.

That conclusion is reinforced by the following link between SSC and the tidal current. The top panel in Fig. 5 shows \tilde{C}_7 , \tilde{C}_{22} and \tilde{C}_{97} from bursts 920 to 928, where the tilde denotes that the data have been low-pass filtered (cutoff period = 10 s). There were low-frequency ($\sim 1/300$ s $^{-1}$) fluctuations in SSC that were highly coherent and in phase across all three measurement levels. Furthermore, SSC was coherent with the low-pass-filtered current direction and speed (bottom panel of Fig. 5). Such fluctuations in SSC and current velocity only occurred, and indeed always occurred, when the tide was flooding and there

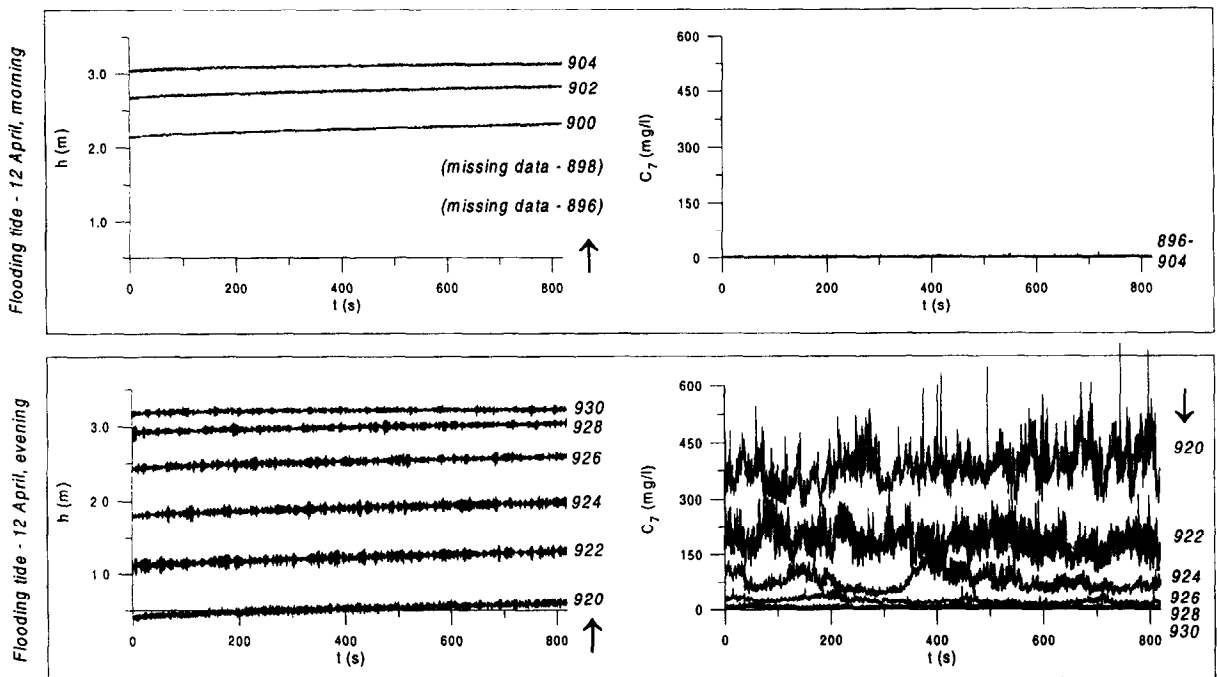


Fig. 4. The top panel shows data from a flooding tide in calm conditions on the intertidal flat. The bottom panel shows data from the next flooding tide, during which a moderate southwesterly wind (mean speed ~ 8 m/s) was raising groupy waves. Each series is one burst of data (13.65 min) with burst numbers indicated (the arrows in each panel show the direction in which time progresses).

were waves. Furthermore, low-frequency fluctuations in current and SSC always occurred together.

No similar signal was evident in the sea-level data; therefore, it is unlikely that the fluctuations were a manifestation of barotropic waves (e.g. basin-wide seiche forced by a change in the wind), and neither did there appear to be any link with wave 'groupiness' (as indicated by a comparison of \tilde{C}_7 , \tilde{C}_{22} and \tilde{C}_{97} with the low-pass-filtered time series of $[h(t) - \bar{h}]^2$; not shown).

Alternative explanations are that the fluctuations relate to an advection or a mixing phenomenon. With the correlation to current direction, the data could be interpreted as indicative of a pulsating 'stream' of turbid water advecting from upstream sources which vary in intensity with direction from the RALPH site. This could include a narrow wave-stirred 'turbid fringe' of the estuarine water body which exhibits a large horizontal concentration gradient across the dominant flow direction. The concentration at the RALPH site would then fluctuate in response to oscillations in

current direction. This scenario offers no explanation for the oscillation in current velocity, however.

Alternatively, eddying arising from interactions of current with morphology or from interactions between waves and currents may manifest as fluctuations in both concentration and current velocity at low frequency. It is interesting in that regard that the meander wavelength is very similar to the downstream component of the wavelength of the linear bars at the edge of the intertidal flat, which suggests that the two are related and that the fluctuations in concentration may relate to vortices shed by bedforms, or to spatial wave-height variations at bar-wavelength spacing.

There were other periods in the deployment when the data were indicative of wave suspension of local bed sediments. Data from one such ebb tide (bursts 2172–2180; evening of May 9) are shown in Fig. 6. These data are different to the data in Fig. 5 in three notable ways. Firstly, there is a significant decrease in burst-averaged SSC between 7 and 97 cm above the bed which is

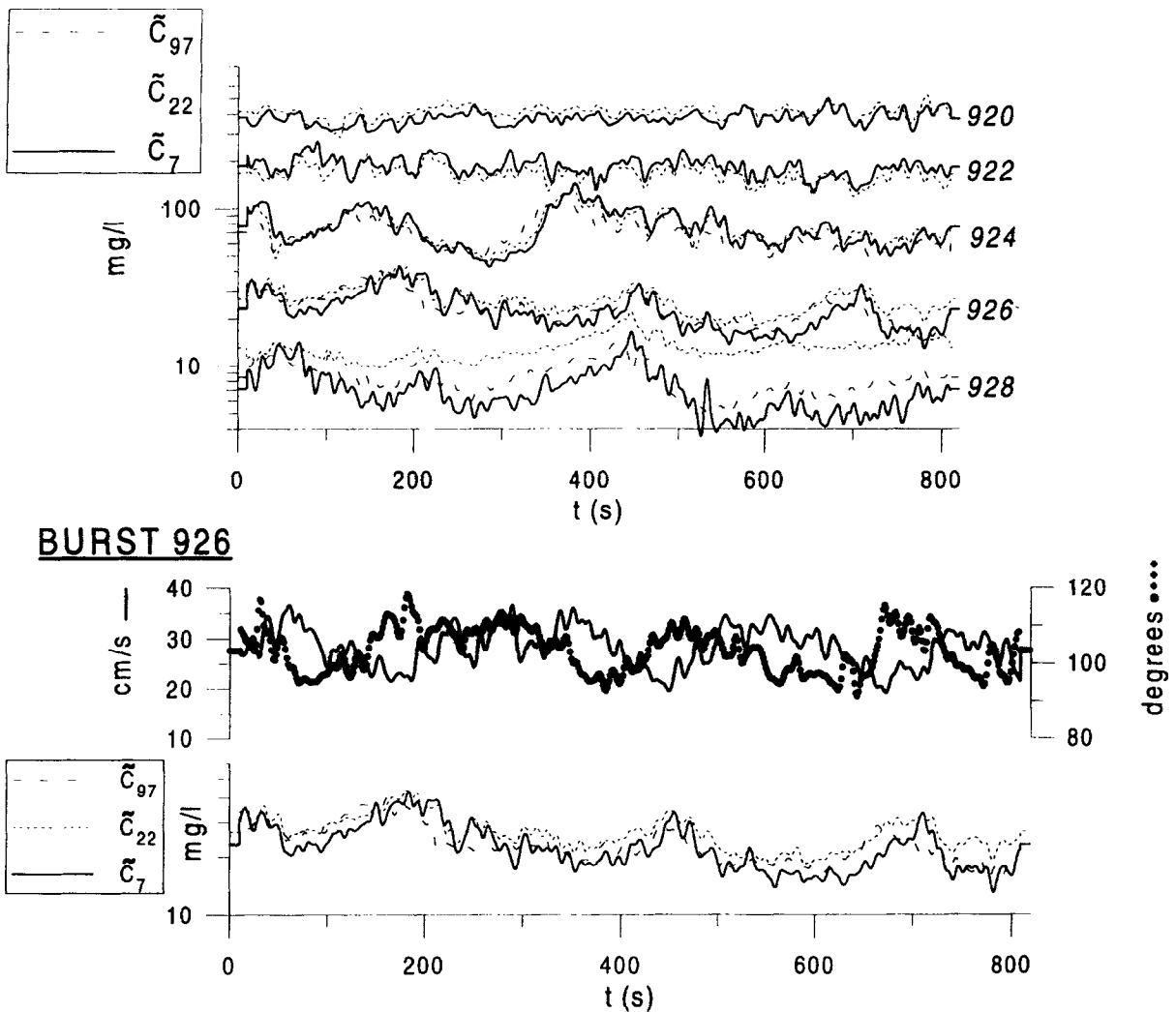


Fig. 5. Top panel: low-pass-filtered SSC at three elevations on a flooding tide with waves present. Bottom panel: low-pass-filtered SSC, current speed and current direction ($z = 48$ cm), burst 926, intertidal flat.

consistent with Eq. (3). Secondly, fluctuations in \tilde{C}_7 and \tilde{C}_{22} are approximately coherent and in phase, but those same fluctuations do not extend to 97 cm above the bed, particularly at high tide (burst 2172). Thirdly, the time scale of the fluctuations in \tilde{C}_7 and \tilde{C}_{22} is similar to the wave-group time scale, with peaks in SSC occurring under wave groups (as indicated by a comparison of \tilde{C}_7 and \tilde{C}_{22} with the low-pass-filtered time series of $[h(t) - h]^2$; shown in Fig. 6 for burst 2176 only). The change in frequency content of the SSC signals with elevation and the relationship between SSC

and wave groupiness are both indicative of wave-induced resuspension of local bed sediments to at least 22 cm above the bed. At 97 cm above the bed the SSC might be principally washload, but note also that the frequency content of \tilde{C}_{97} changed with the change in water depth.

4.2.3. Variation in waves and wave suspension of bed sediments over the tidal cycle

When 'turned on', wave growth and the associated suspension of bed sediments varied markedly over the tidal cycle, as follows.

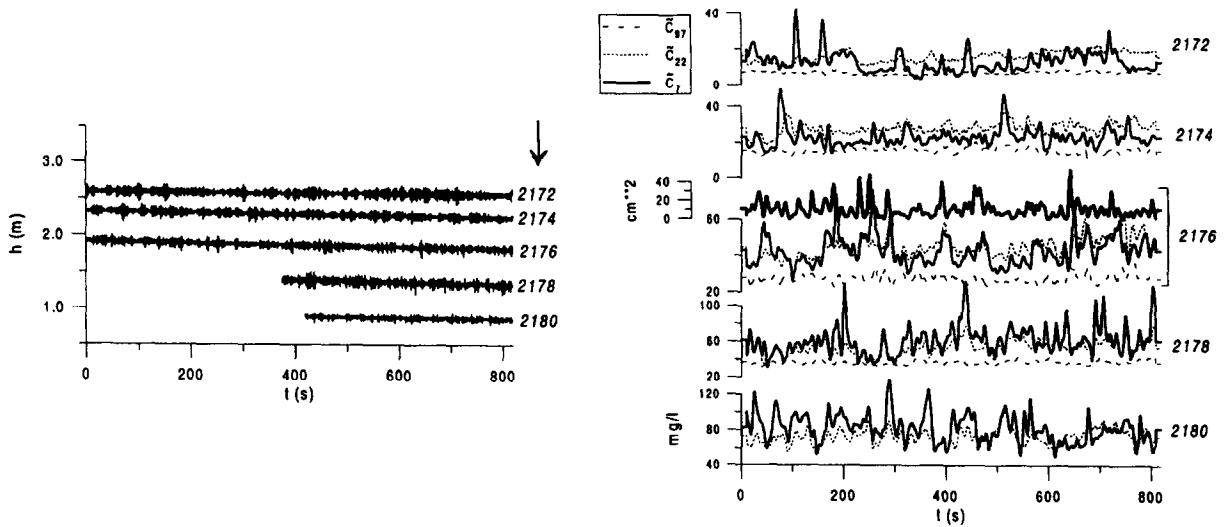


Fig. 6. Data from an ebbing tide with waves present. Bursts 2172 to 2180, intertidal flat. On the left is water depth, on the right is low-pass-filtered SSC at three elevations. Low-pass-filtered 'wave amplitude' (i.e. $[h(t) - \bar{h}]^2$, units of cm^2) is shown for burst 2176.

Fig. 7 shows variation in waves and wave-orbital currents over a tidal cycle. Throughout the rise and fall of the tide, the estuarine geometry, wind strength and intrinsic properties of waves governed H_{sig} and $U_{\text{sig,b}}$ at the RALPH site, as follows. H_{sig} varied in phase with the water depth, such that H_{sig} increased/decreased as \bar{h} increased/decreased, except near high tide, when H_{sig} decreased for a short time. A wave-generation model adapted to wave growth in an enclosed sea under an unsteady wind (WGEN3DD; Black et al., 1997) demonstrated that the variation in H_{sig} that was in phase with \bar{h} was driven by the change in fetch associated with the harbour-wide submergence and emergence of sandbanks that accompanied the rise and fall of the tide. The decrease in H_{sig} at high tide was related to the momentary decrease in wind speed that occurred at that time. In contrast, the variation over the tidal cycle in $U_{\text{sig,b}}$ was more complicated, which is because that variation depends on the relative changes in H_{sig} and \bar{h} . $U_{\text{sig,b}}$ was lowest around high tide, which is a simple consequence of the fact that orbital motions decay with depth under transitional and deep-water waves. $U_{\text{sig,b}}$ attained a maximum around mid-tide, at which time the combination of wave height and water depth was optimum for generating largest orbital velocities at the bed.

That is, when the water was deeper, waves were higher but penetration of orbital motions to the bed was less, and when the water was shallower, penetration was greater but waves were lower.

\bar{C}_7 was smallest at high tide and largest around low tide (Fig. 7). Although \bar{C}_7 apparently changed smoothly between low and high tide, further analysis using the Nielsen (1986) model for the wave-related suspended-sediment reference concentration (i.e. \bar{C}_0 ; the time-averaged SSC at the level of the bed) suggests that fundamental changes in the suspension dynamics occurred, as shown in Fig. 8. Fig. 8 shows $\bar{C}_7/e^{-7/\lambda_s}$ plotted against \bar{C}_0 for bursts 2156 to 2188 (the same bursts plotted in Fig. 7). $\bar{C}_7/e^{-7/\lambda_s}$ is the 'observed' reference concentration, which is \bar{C}_7 extrapolated to the bed using Eq. (3) and assuming a mixing length of 10 cm (described previously). \bar{C}_0 is the 'predicted' reference concentration using the Nielsen (1986) model:

$$\bar{C}_0 = 0.005 \rho_s \{0.5 f_w \rho_f U_M^2 / [(\rho_s - \rho_f) g D]\}^3 \quad (4)$$

where:

$$U_M = 1.4 \left[\sum_{j=1}^N U_{17,j}^M / N \right]^{1/M} \quad (5)$$

and N is the number of points in a data burst and

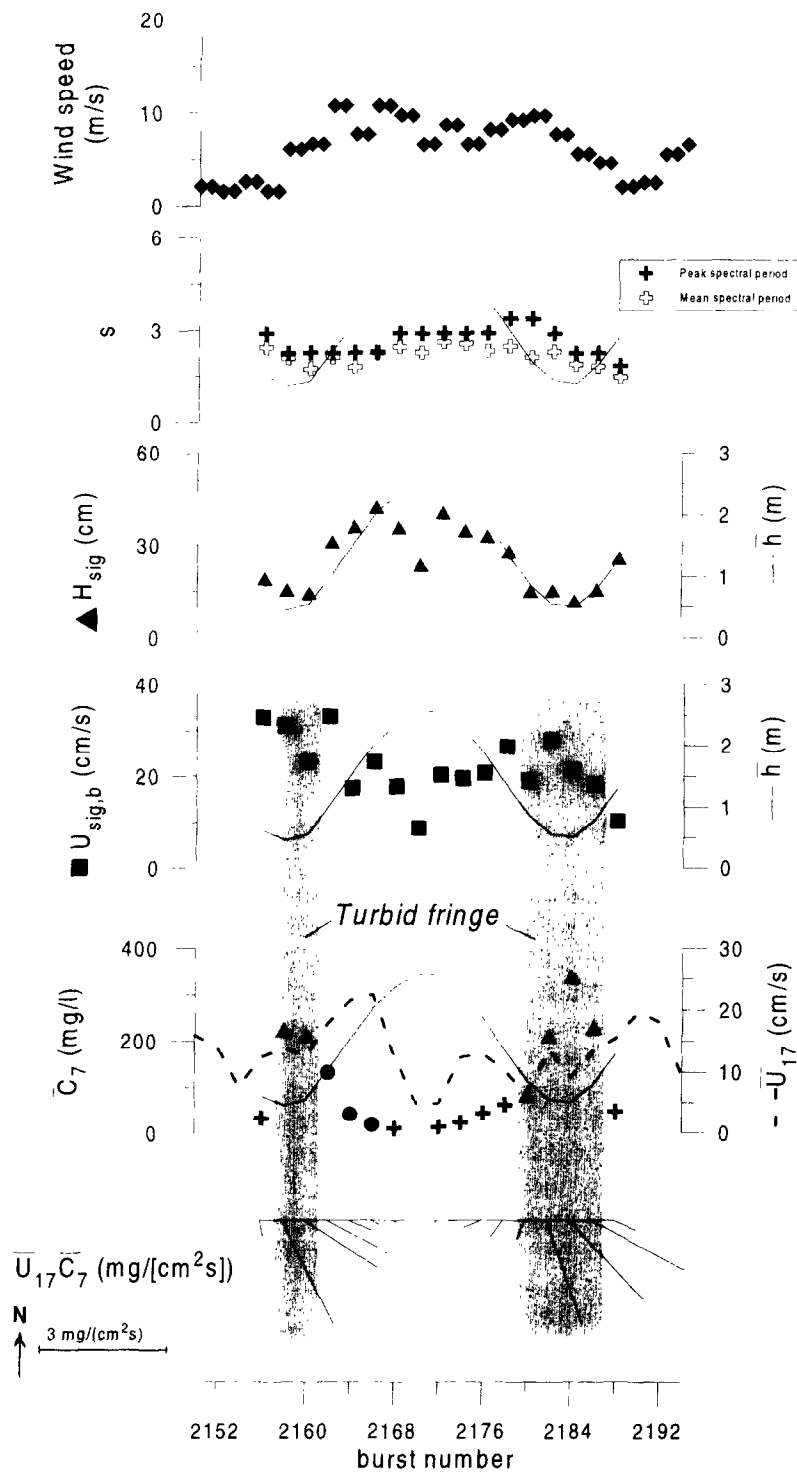


Fig. 7. Wind speed, wave period, wave height, wave-orbital speed, SSC at 7 cm above the bed, current speed and mean flux of suspended sediment during a tidal cycle with a wind blowing from the southwest across a large fetch. Intertidal flat, bursts 2156 to 2188.

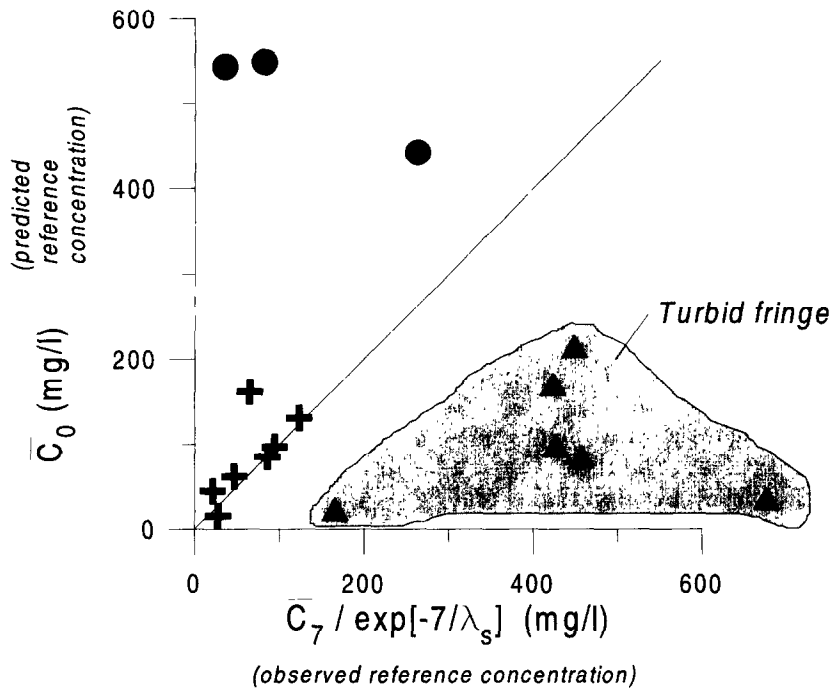


Fig. 8. Data from a tidal cycle with a wind blowing from the southwest across a large fetch. Intertidal flat, bursts 2156 to 2188. Predicted suspended-sediment reference concentration (Eq. (5), with $M=3$) versus observed reference concentration (C_7 extrapolated to the bed using Eq. (3) and assuming a mixing length of 10 cm).

$M=3$. f_w is the wave friction factor, given by Swart (1974) as:

$$f_w = \exp[5.213(2.5D/a_b)^{0.194} - 5.977] \quad (6)$$

where a_b is the orbital semi-excursion defined as $U_M \bar{T}$, and ρ_s is the sediment density (2.65 g/cm^3), ρ_f is the fluid density (1.0 g/cm^3), D is the sediment grain size (0.1 mm) and g is acceleration due to gravity. $U_{M=3}$ corresponds to the 92nd percentile of the velocity distribution, which was used by Kosyan (1985) to predict time-averaged SSC under irregular waves; U_M can be thought of as the 'representative' orbital current under irregular waves (Black and Rosenberg, 1991). We have taken the current measured at 17 cm above the bed to define the wave orbital motion near the bed in Eq. (5).

The data plotted in Fig. 8 fall into three groups. In the first group (shown by crosses in Figs. 7 and 8), Nielsen's model was found to provide a good description of the relationship between SSC and

the wave-orbital current. The bursts in this group are from the falling tide, and include the same bursts that were shown in Fig. 6 to demonstrate suspension of local bed sediments by waves.

In the second group (shown by triangles in Figs. 7 and 8), observed SSC is much greater than predicted SSC. The bursts in this group are from near low tide, which was when the suspended-sediment load was in fact highest. These bursts correspond to the presence at the RALPH site of a relatively narrow (50–100 m) zone of highly turbid, shallow (<1 m) water at the edge of the estuarine water body. The sediment load in this 'turbid fringe' may be maintained by the advance and retreat of the shallow edge of the water body with the tide. Alternatively, the high turbidity could be maintained by penetration to the bed from the surface of turbulence associated with breaking waves. At the RALPH site, the water depth in the turbid fringe was 1.5–2 times greater than the depth at which the measured waves were

expected to break using the Madsen (1976) model. However, the exceptionally small bed slopes at the Wiroa Island site and the following wind could have caused white-capping and turbulence levels to rise. In any case, the relationship between turbidity and wave-orbital velocity is markedly different in the turbid fringe than in the first group of bursts mentioned above, which is suggestive of fundamental differences in hydrodynamics or entrainment mechanism.

In the third group (shown by circles in Figs. 7 and 8), the observed SSC was much smaller than the predicted SSC. The bursts in this group are from the rising tide, which was when there was a strong low-frequency fluctuation in the SSC and a corresponding low-frequency signal in the current velocity. The data in Fig. 8 suggest that wave suspension of bed sediment at the RALPH site was suppressed at these times, but we can think of no plausible explanation as to why that should be so.

4.2.4. Suspended-sediment flux

Sediment transport or flux is the product of current speed and SSC. Typically, the magnitude of the sediment flux at elevation z above the bed is estimated as $\bar{U}_z \bar{C}_z$ with direction of flux assumed to be parallel to the mean current. $\bar{U}_z \bar{C}_z$ is actually the rate at which the mean SSC is advected by the mean current, and is not necessarily equivalent to the total flux of sediment if $U(t)$ and $C(t)$ are correlated at one or more frequencies (e.g. Vincent and Green, 1990). We have already identified fluctuations that appear from time-to-time in both $U(t)$ and $C(t)$ at a 'meander' frequency and in the surface-gravity-wave frequency band. Thus, in order to analyse sediment transport, we decompose the total sediment flux into three components:

$$\begin{aligned} \overline{U_z C_z} &= (\overline{U_{w,z}} + \overline{U_{m,z}} + \overline{U_z})(\overline{C_{w,z}} + \overline{C_{m,z}} + \overline{C_z}) \\ &= \overline{U_{w,z} C_{w,z}} + \overline{U_{m,z} C_{m,z}} + \overline{U_z C_z} \end{aligned} \quad (7)$$

where $\overline{U_z C_z}$ is the magnitude of the total sediment flux at elevation z above the bed, the first term on the right-hand side is the magnitude of the sediment flux carried by surface-gravity waves (periods of 2–30 s), the second term is the magnitude of the sediment flux carried in the meandering stream previously identified as being linked to the linear

bars at the RALPH site (periods > 30 s), and the third term is the mean flux as previously mentioned. For the purposes of evaluating Eq. (7)

$$\overline{U_{w,z}} = \sqrt{\int_{1/2}^{1/30} S_{U_z}(f) df},$$

$$\overline{C_{w,z}} = \sqrt{\int_{1/2}^{1/30} S_{C_z}(f) df},$$

$$\overline{U_{m,z}} = \sqrt{\int_{1/30}^{1/N\Delta t} S_{U_z}(f) df} \text{ and}$$

$$\overline{C_{m,z}} = \sqrt{\int_{1/30}^{1/N\Delta} S_{C_z}(f) df}$$

where N is the number of points per burst, Δt is the sampling interval and $S(f)$ is the autospectrum with f being frequency.

On the intertidal flat, where there was marked variation in SSC and current speed over the tidal cycle, the mean flux $\overline{U_{17}} \overline{C_7}$ was controlled by the relative phases of $\overline{U_{17}}(t)$ and $\overline{C_7}(t)$, where the time average is over the burst but t now signifies time on the order of hours. This is demonstrated in Fig. 7 for bursts 2156–2188, in which it is seen that $\overline{U_z} \overline{C_z}$ close to the bed was greatest in the turbid fringe, in which $\overline{C_7}$ was high but $\overline{U_{17}}$ was not maximum.

The flux associated with surface gravity waves $\overline{U_{w,17}} \overline{C_{w,7}}$ was about 10–15% of the mean flux $\overline{U_{17}} \overline{C_7}$ when waves were actively suspending local bed sediments (e.g. during bursts 2172 to 2180, see Fig. 6). At 97 cm above the bed, the wave flux was virtually zero. Close to the bed, wave-orbital motions carried sediment in the direction of wave advance, which was parallel to the wind. During ebbing tides, the wave flux under southwesterly winds typically opposed the mean flux and thus the total sediment flux close to the bed was diminished by the transport of sediment by the waves.

The flux associated with the meander ($\overline{U_{m,17}} \overline{C_{m,7}}$) when there was a pronounced low-frequency fluctuation in the current velocity and similar low-frequency oscillations in the SSC (e.g. during bursts 920 to 928, see Fig. 5) was never more than a few percent of the mean flux $\overline{U_{17}} \overline{C_7}$. However, the meander flux was consistently

directed offshore and parallel to the crests of the linear bars.

4.2.5. Boundary-layer dynamics

The inertial-dissipation method (Batchelor, 1950; Tennekes and Lumley, 1972) was used to estimate the time-averaged bed shear stress, $\bar{\tau}_b$, from the inertial subrange of the current-speed energy spectrum measured at 17 cm above the bed (for a detailed description of the method, see Green, 1992; Green and McCave, 1995). The method is valid for neutrally stratified flow and for current measurements made in the constant-stress region of the benthic boundary layer, and includes a correction for current measurements made below a critical level in the flow (Huntley, 1988). $\bar{\tau}_b$ was substituted together with \bar{U}_{17} into the law-of-the-wall (e.g. Daily and Harleman, 1966) to obtain estimates of the hydraulic roughness, Z_0 , and the drag coefficient referenced to 100 cm above the bed, $C_{D,100}$:

$$Z_0 = \exp[\ln(17) - (\kappa \bar{U}_{17} / U_*)] \quad (8)$$

$$C_{D,100} = \left[\frac{\kappa}{\ln(100/Z_0)} \right]^2 \quad (9)$$

where Z_0 is in centimetres, κ is von Karman's constant, and $U_* = (\bar{\tau}_b / \rho_f)^{1/2}$ is the friction velocity.

Analysis of the drag estimates reveals the significant role of wave-current interaction in the benthic boundary layer, as follows.

Z_0 at the RALPH site was found to be approximately constant at ~ 0.05 cm ($C_{D,100} = 0.0028$; similar to the 'traditional' steady-flow value of 0.0025, e.g. Dronkers, 1964) throughout the tidal cycle when there were no waves. In contrast, in the presence of waves, Z_0 varied markedly over the tidal cycle (Fig. 9). Fig. 9 shows that changes in Z_0 paralleled changes in the ratio $U_{\text{sig},b} / \bar{U}_{17}$, and that Z_0 in the wave-current flow always exceeded Z_0 without waves. Thus, the data reflect the effects of boundary-layer wave-current interaction (e.g. Grant and Madsen, 1986; Huntley and Hazen, 1988; Green et al., 1990). The maximum measured Z_0 in the combined flow was ~ 0.1 m, which implies $k = \sim 3$ m at that time. Thus, although the waves on the intertidal flat were small, the hydraulic roughness under the wave-plus-current was

large, and indeed as large as roughness measured over bedforms on the continental shelf under combined ocean swell and currents (e.g. Black et al., 1996).

Assuming that the boundary-layer flow was fully rough-turbulent at all times, in which case $Z_0 = k/30$ where k is the physical bed roughness (which encompasses the sediment texture and the bedforms), the constant value of Z_0 in the absence of waves implies unchanging bedforms. The enhanced roughness in the combined flow is reflected in the ratio:

$$(\bar{\tau}_b / \rho_f)^{1/2} / (\kappa \bar{U}_{17} / \ln[17/0.05])$$

i.e. the observed time-averaged bed shear stress in the combined wave-current flow normalised by the calculated time-averaged bed shear stress for a pure current with the same speed and bed roughness that is characteristic of the RALPH site without waves (i.e. $Z_0 = 0.05$ cm). The time-averaged bed shear stress was as much as 3.75 times greater in the wave-current flow (Fig. 9).

The lowest optical backscatter sensor was 7 cm above the bed, too high to detect bedload sediment transport. However, the stress data indicate that tidal currents were incapable of initiating extensive bedload movement, as follows. With Z_0 equal to 0.05 cm, the maximum observed \bar{U}_{17} of ~ 30 cm/s translates into a $\bar{\tau}_b$ in the absence of waves of $\sim 4.5 \text{ g s}^{-2} \text{ cm}^{-1}$, which is equivalent to a non-dimensional bed shear stress (θ) of 0.28, where:

$$\theta = \frac{\bar{\tau}_b}{(\rho_s - \rho_f)gD} \quad (10)$$

with $\rho_s = 2.65 \text{ g/cm}^3$ and $D = 0.1$ mm. Z_0 estimated from the velocity data reflects both sediment and ripple roughness, and thus a part of the bed shear stress estimated using 0.05 cm for Z_0 is related to form drag around bedforms, which dissipates energy independently of the viscous drag on sediment grains (i.e. skin friction). The skin friction $\bar{\tau}'_b$ can be estimated using $Z_0 = 2.5D/30$ in the law-of-the-wall, which reflects the grain roughness only. Doing that yields $\bar{\tau}'_b = 1.5 \text{ g s}^{-2} \text{ cm}^{-1}$ ($\theta' = 0.095$) for \bar{U}_{17} of 30 cm/s, which is slightly less than 0.10, the critical non-dimensional stress for initiation of sediment motion as bedload (θ_{cr})

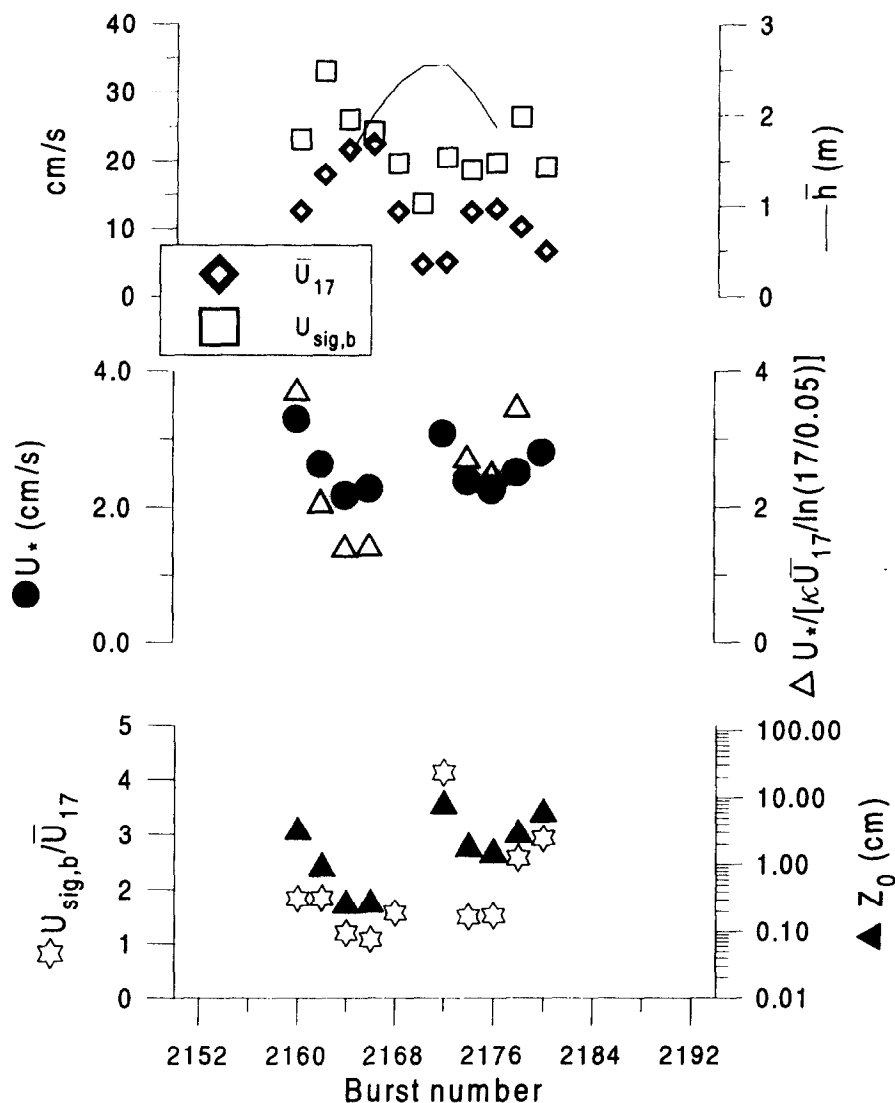


Fig. 9. Data from a tidal cycle with a wind blowing from the southwest across a large fetch. Intertidal flat, bursts 2156 to 2188. Parameters related to boundary-layer dynamics.

corresponding to $D=0.1$ mm (Madsen and Grant, 1976).

5. Discussion

At first glance, measurements of sediment transport in Papakura Channel (Fig. 2) look easy to understand and model, but that impression is deceptive. During ebbing tides, some significant

proportion of the suspended-sediment load passing around the S4A apparently derived from upstream, but during flooding tides the suspended-sediment load apparently derived more from the local seabed. Thus, ebb- and flood-tide sediment transport at the level of the S4A differ fundamentally in character, which implies that time series of SSC and current velocity need to be divided according to tidal phase prior to analysis. In addition, both ebb- and flood-tide processes may be non-station-

ary on a spring–neap scale, which will further complicate time-series analysis.

Although there is emphasis on flood and ebb dominance in the literature as a guide to understanding estuarine morphodynamics, the variability in net load integrated over a tidal cycle suggests that an equally relevant question must be: what is the upstream sediment-transporting capacity (including that contributed by waves) and the time scale of sediment deposition for the grain sizes being suspended? The concepts of sediment ‘availability’ (e.g. Black, 1987; Black et al., 1989), sediment-transporting capacity and settlement time scales are critical to an understanding of the total loads that advect through estuaries. In the Manukau Harbour, the intensity of tidal currents is only one part of the sediment-transporting capacity; wave action along flow streamlines extending upstream of a measurement site might additionally raise SSC at that site. Since waves in Manukau are locally generated, largest waves occur on downwind shorelines and the location of the largest waves will vary continuously as the wind rotates. Ebb- and flood-dominance in channels may be altered accordingly. Such considerations demonstrate that tidal-current strength alone is not necessarily indicative of net sediment transport. Variations in tidal-current intensity and near-bed wave-orbital motions acting on a range of grain sizes along the flow streamlines will ultimately determine net transport. Where fine material is available and the settlement times are long, the local SSC may be greatly enhanced by waves on a distant intertidal flat. Simulations with a three-dimensional, particle-tracking numerical model that accounts for nonuniform bed sediment will aid understanding of channel sediment transport.

Tidal currents acting alone were not capable of entraining sediment on the Wiroa Island intertidal flat at the RALPH site, even as bedload. Many lines of evidence gleaned from the RALPH data demonstrate the important role of waves on the intertidal flat: the switching on and off of turbidity with waves (Fig. 4); the correlation of fluctuations in SSC with fluctuations in current speed at the wave-group scale (Fig. 6); the appearance of the dominant bedforms at the RALPH site; the indica-

tors of wave–current interaction in the benthic boundary layer (Fig. 9); and the good performance (at times) of Nielsen’s equation for predicting suspended-sediment reference concentration (Fig. 8). Both the waves themselves and the wave-related processes (e.g. generation of combined-flow bed shear stress and hydraulic roughness, sediment resuspension) showed marked variation over the tidal cycle.

The variation over the tidal cycle in the waves themselves (principally changes in height) was related to changes in the fetch caused by emergence and submergence of sandbars and to slight variations in the wind strength. The variation over the tidal cycle in wave-related processes was related to changes in kh , which affected penetration of wave-orbital motions to the bed, and which were driven mainly by tidal variation in local water depth. Thus, the former represents a change in the wave train itself, but the latter is due to intrinsic properties of the waves. Both factors could only be adequately modelled within an estuary tidal model that accounts for tidal variation in estuarine geometry and water depth.

Little attention has been paid in the past to variations over the tidal cycle in wave-related processes on intertidal flats, which is somewhat surprising since, under short-period waves that are characteristic of estuaries, kh can vary across the entire deep-water–shallow-water range in just a matter of hours and have profound effects on sediment dynamics. In addition to the variation over the tidal cycle in ‘intensity’ of wave-driven processes, there was also a change in ‘kind’, which occurred with the arrival of the turbid fringe and the associated radical change in the relationship between turbidity and wave-orbital velocity (Fig. 8), which implied a change in dynamics, perhaps related to breaking waves.

Although waves control the amount of bed sediment that is resuspended on the intertidal flat (as expressed by the reference concentration), it is the steady (i.e. tidal) current that controls the horizontal flux of suspended sediment through the deployment site. That is, $\bar{U}_{17}\bar{C}_7$ was the largest term in the expansion of $\bar{U}_{17}\bar{C}_7$. Although \bar{U}_{17} and \bar{C}_7 varied systematically over the tidal cycle, they are not linked in any fundamental way: the

former is the tidal current, which is driven by the basin-wide pressure gradient, and the latter is driven by wave-orbital motions at the seabed, which vary because of changes in the wave train itself and in the water depth. Although not as large as $\overline{U_z C_z}$, the other terms in the expansion of $\overline{U_z C_z}$ may play important roles as well. For instance, $\overline{U_{w,z} C_{w,z}}$ (the wave flux) decayed rapidly with elevation above the bed, which could act to preferentially transport coarser grains that are not lifted far from the bed, and the measurements showed a net movement in the direction of wave propagation, which, during the ebbing tide, was nearly opposite to the mean flux. The meander flux ($\overline{U_{m,17} C_{m,17}}$) may be due to a feature of the large-scale morphology of the intertidal flat, viz. the linear bars at the edge of the intertidal flats. It is possible to distinguish between wave-driven local suspension and advection of sediment from a distant source by examining the decay with elevation above the bed of time-averaged SSC and the frequency content of SSC time series.

The acquisition of accurate, quantitative SSC data is problematic in an estuary with multiple sediment sources that vary in grain size and composition. The reason is that both optical and acoustic backscatter sensors used for measuring SSC respond differently to different sediment types. The interpretation of the optical backscatter data herein has been hampered by uncertainty in the instrument calibration and by the possibility that the grain size of the suspended sediment changes over the tidal cycle. The problem might be resolved in the future by using combinations of optical and acoustic sensors (e.g. Green and Boon, 1993) or multiple-frequency acoustic devices (e.g. Thorne et al., 1991).

6. Conclusions

Sediment dynamics on the intertidal flat is controlled by waves, which occur intermittently. However, when waves are present, there is a characteristic continuous variation over the tidal cycle in processes controlling sediment transport. This suggests that a 'hybrid' modelling approach is required, i.e. one that treats discrete events but

resolves tidal-cycle-scale variation within the event. Our analysis points the way towards model requirements. Included in these are the need to resolve the variation in the wave train over the tidal cycle and the penetration to the bed of wave-orbital motions, both of which could only be done adequately within an estuary tidal model. It is also necessary to account for wave–current interaction in the benthic boundary layer and to resolve the vertical distribution of suspended-sediment flux. To predict suspended-sediment loads, we need to know the upstream sediment-transporting capacity (including that due to waves), the character and basin-wide distribution of bed sediments and the time scale of sediment deposition for the grain sizes being suspended. Factors to consider are the rotating wind, the definition of 'upstream', tidal strength along the flow streamline, sediment availability and total sediment-transporting capacity, including that contributed by waves. These factors interact to confound the simplest notion of ebb and flood dominance. More detailed measurements combined with a three-dimensional, particle-tracking sediment-transport model that accounts for nonuniform sediment distribution in the estuary are required to resolve the problem.

Progress towards answering fundamental questions such as how sediment is exchanged between channels and intertidal flats and what is the source and fate of sediment that passes along the channel, will be made by using three-dimensional numerical-model simulations that account for the range of processes and interactions that have been elucidated from the Wiroa Island dataset.

Acknowledgements

We thank Dave Heffler of the Geological Survey of Canada (GSC) for keeping RALPH running under trying conditions, and Dick Pickrill (GSC) and Rick Pridmore (NIWA) for supporting the collaboration between NIWA and GSC. Thanks also to Tony Dolphin, Rod Budd, Rob Bell and John Oldman for help in the field, to Rob Bell for comments on the manuscript, and to the journal reviewers. The work was funded by the New

Zealand Foundation for Research, Science and Technology.

References

- Amos, C.L., Tee, K.T., 1989. Suspended sediment transport processes in Cumberland Basin. *J. Geophys. Res.* 94, 14407–14417.
- Anderson, F.E., 1972. Resuspension of estuarine sediments by small amplitude waves. *J. Sediment. Petrol.* 42 (3), 602–607.
- Batchelor, G.K., 1950. The application of the similarity theory of turbulence to atmospheric diffusion. *Q. J. R. Meteorol. Soc.* 76, 133–146.
- Beach, R.A., Sternberg, R.W., 1988. Wave–current interactions in the inner surf zone and their influence on suspended sediment transport. In: IAHR Symp. Mathematical Modelling of Sediment Transport in the Coastal Zone. Danish Hydraulics Institute, Copenhagen, pp. 155–165.
- Bendat, J.S., 1958. Principles and Applications of Random Noise Theory. John Wiley, London, 431 pp.
- Black, K.P., 1987. A numerical sediment transport model for application to natural estuaries, harbours and rivers. In: J. Noye (Ed.), Numerical Modelling Applications to Marine Systems. Mathematics Studies 145, North Holland/Elsevier, Amsterdam, pp. 77–105.
- Black, K.P., Rosenberg, M.A., 1991. Suspended load at three time scales. Coastal Sediments '91. A.S.C.E. Waterway, Port, Coastal and Ocean Division 1, pp. 313–327.
- Black, K.P., Healy, T.R., Hunter, M., 1989. Sediment dynamics in the lower section of a mixed sand and shell-lagged tidal estuary. *J. Coastal Res.* 5 (3), 503–521.
- Black, K., Rosenberg, M., Symonds, G., Simons, R., Pattiaratchi, C., Nielsen, P., 1996. Measurements of wave, current and sea level dynamics of an exposed coastal site. In: Pattiaratchi, C. (Ed.), Mixing Processes in Estuaries and Coastal Seas. Am. Geophys. Union, Washington, D.C., Ch. 2, pp. 29–58.
- Black, K.P., Healy, T., Green, M.O., Bell, R.G., Oldman, J.W., Hume, T.M., 1997. Lagrangian modelling techniques simulating wave and sediment dynamics determining sand-body equilibria. In: Harff, J., (Ed.), Computerized Modelling of Sedimentary Systems. Springer, Berlin, in press.
- Daily, J.W., Harleman, D.R.F., 1966. Fluid Dynamics. Addison-Wesley, Reading, MA, 454 pp.
- Dolphin, T.J., 1992. Low Amplitude Multiple Bar Systems in a Fetch Limited Intertidal Environment. M.Sc. Thesis, Univ. Auckland, 143 pp. (Unpubl.)
- Dolphin, T.J., Hume, T.M., Parnell, K.E., 1995. Oceanographic processes and sediment mixing on a sand flat in an enclosed sea, Manukau Harbour, New Zealand. *Mar. Geol.* 128, 169–181.
- Dronkers, J.J., 1964. Tidal Computations in Rivers and Coastal Waters. North-Holland, New York.
- Grant, W.D., Madsen, O.S., 1986. The continental shelf bottom boundary layer. *Ann. Rev. Fluid Mech.* 18, 265–305.
- Green, M.O., 1992. Spectral estimates of bed shear stress at subcritical Reynolds numbers in a tidal boundary layer. *J. Phys. Oceanogr.* 22 (8), 903–917.
- Green, M.O., Boon, J.D., 1993. The measurement of constituent concentrations in nonhomogeneous sediment suspensions using optical backscatter sensors. *Mar. Geol.* 110, 73–81.
- Green, M.O., McCave, I.N., 1995. Seabed drag coefficient under tidal currents in the eastern Irish Sea. *J. Geophys. Res.* 100 (C8), 16057–16069.
- Green, M.O., Rees, J.M., Pearson, N.D., 1990. Evidence for the influence of wave–current interaction in a tidal boundary layer. *J. Geophys. Res.* 95 (C6), 9629–9644.
- Heath, R.A., Greig, M.J.N., Shakespeare, B.S., 1976. Circulation and hydrology of the Manukau Harbour, New Zealand. *J. Mar. Freshwater Res.* 11 (3), 589–607.
- Huntley, D.A., 1988. A modified inertial dissipation method for estimating seabed stresses at low Reynolds numbers, with application to wave–current boundary-layer measurements. *J. Phys. Oceanogr.* 18, 339–346.
- Huntley, D.A., Hazen, D.G., 1988. Seabed stresses in combined wave and steady flow conditions on the Nova Scotia continental shelf: field measurements and predictions. *J. Phys. Oceanogr.* 18, 347–362.
- Jarvis, J., Riley, C., 1987. Sediment transport in the mouth of the Eden estuary. *Estuarine Coastal Shelf Sci.* 24, 463–481.
- Kestner, F.J.T., 1975. The loose-boundary regime of the Wash. *Geogr. J.* 141, 389–412.
- Kosyan, R.D., 1985. Vertical distribution of suspended sediment concentrations seawards of the breaking zone. *Coastal Eng.* 9, 171–187.
- Longuet-Higgins, M.S., 1975. On the joint distribution of periods and amplitudes of sea waves. *J. Geophys. Res.* 80 (18), 2688–2694.
- Madsen, O.S., 1976. Wave climate of the continental margin: elements of its mathematical description. In: Stanley, D.J., Swift, D.J.P. (Eds.), Marine Sediment Transport in Environmental Management. Wiley, New York, NY, pp. 65–87.
- Madsen, O.S., Grant, W.D., 1976. Sediment Transport in the Coastal Environment. Report 209, Ralph M. Parsons Lab., Dep. Civ. Eng., Mass. Inst. Technol., Cambridge, MA, 105 pp.
- Nielsen, P., 1984. Field measurements of time-averaged suspended sediment concentrations under waves. *Coastal Eng.* 8, 51–72.
- Nielsen, P., 1986. Suspended sediment concentration under waves. *Coastal Eng.* 10, 23–31.
- Pethick, J., 1984. An Introduction to Coastal Geomorphology. Edward Arnold, London.
- Postma, H., 1967. Sediment transport and sedimentation in the estuarine environment. In: Lauff, G.M. (Ed.), Estuaries. AAAS Publ. 83, 158–179.
- Shoellhamer, D.H., 1995. Sediment resuspension mechanisms in Old Tampa Bay, Florida. *Estuarine Coastal Shelf Sci.* 40, 603–620.
- Swart, D.H., 1974. A schematization of onshore–offshore trans-

- port. Proc. 14th Int. Conf. Coastal Eng., Am. Soc. Civ. Eng., New York, pp. 884–900.
- Tennekes, H., Lumley, J.L., 1972. *A First Course in Turbulence*. MIT Press, 300 pp.
- Thorne, P.D., Vincent, C.E., Hardcastle, P.J., Rehman, S., Pearson, N.D., 1991. Measuring suspended sediment concentrations using acoustic backscatter devices. *Mar. Geol.* 98, 7–16.
- Vincent, C.E., Green, M.O., 1990. Field measurements of the suspended sand concentration profiles and fluxes of the resuspension coefficient γ_0 over a rippled bed. *J. Geophys. Res.* 95, 11591–11601.
- Ward, L.G., Kemp, W.M., Boynton, W.R., 1984. The influence of waves and seagrass communities on suspended particulates in an estuarine embayment. *Mar. Geol.* 59, 85–103.